Magnetically Detected Protein Binding Using Spin-labeled Slow Off-rate Modified Aptamers

Shutian Lu,[†] Catherine R. Fowler,[‡] Brian Ream,[‡] Sheela M. Waugh,[‡] Theresa M. Russell,[‡] John C. Rohloff,[‡] Larry Gold,[‡] Jason P. Cleveland ,[‡] and Stefan Stoll[*,†]

†*Department of Chemistry, University of Washington, Seattle, Washington 98195, United States*

‡*SomaLogic, Boulder, Colorado 80301, United States*

E-mail: stst@uw.edu

Abstract

Recent developments in aptamer chemistry open up opportunities for new tools for protein biosensing. In this work, we present an approach to use immobilized slow off-rate modified aptamers (SOMAmers) site-specifically labelled with a nitroxide radical via azide–alkyne click chemistry as a means for detecting protein binding. Protein binding induces a change in rotational mobility of the spin label, which is detected via solution-state electron paramagnetic resonance (EPR) spectroscopy. We demonstrate the workflow and test the protocol using the SOMAmer SL5 and its protein target, platelet-derived growth factor B (PDGF-BB). In a complete site scan of the nitroxide over the SOMAmer, we determine the rotational mobility of the spin label in the absence and presence of target protein. Several sites with sufficiently tight affinity and large rotational mobility change upon protein binding are identified. We then model a system where the spin-labeled SOMAmer assay is combined with fluorescence detection via diamond nitrogen–vacancy (NV) center relaxometry. The NV center spin–lattice relaxation time is modulated by the rotational mobility of a proximal spin label and thus responsive to SOMAmer–protein binding. The spin label-mediated assay provides a general approach for transducing protein binding events into magnetically detectable signals.

Keywords: aptamer, protein assay, EPR spectroscopy, spin labeling, quantum sensing

Regular and complete proteomics panels can provide real-time diagnostic insight into human health and enable preventive and early treatments of nascent disease states.[1,2] Such measurements must be reliable and require fast, accurate and accessible multi-protein sensors. Novel designs for such sensors featuring small sample volumes and high sensitivity have become feasible due to the recent developments in aptamer chemistry and quantum technologies.[3–5] A special class of DNA aptamers known as slow off-rate modified aptamers (SOMAmers) have been used as molecular binding reagents in a variety of biochemical studies.[6–9] SOMAmers are selected for tight binding interaction to target proteins and contain a series of nucleobases modified using hydrophobic constituents such as benzene and naphthalene rings.[10] The incorporation of these modifications has been demonstrated to improve the binding specificity and affinity of SOMAmers. With these properties, SOMAmers are reliable agents for capturing traces of specific target proteins.[11,12] In general, the SOMAmers are selected to form tight interactions with their targets with K_d values in the range of several nM to pM.[13–16] Structural information has been obtained from several SOMAmer–protein complexes.[6,17–19]

The specificity and affinity of SOMAmer–protein interactions can be fully utilized if they are paired with sensitive detection methods, ideally at the single-molecule level. One option for such a quantum sensor is the negatively charged nitrogen–vacancy (NV) center in diamond. The NV center is a defect color center with a spin-triplet ($S = 1$) ground state localized on the dangling carbon bonds next to the vacancy. It can be spin polarized via optical pumping and provides a spin-sensitive fluorescence readout. The use of the NV center as a quantum sensor for local magnetic fields is well studied.[20–22] Numerous studies have demonstrated the ability of NV centers to detect the presence of proximal spin species, such as proton spins on the diamond surface,[23] proton spins in the solvent[24–26] and single electron spin centers in proximal biomolecules.[27–32]

There are several challenges that must be overcome in order to integrate SOMAmers and NV center-mediated detection into a device for protein sensing. One is to develop a biocompatible surface on NV center-hosting diamond for SOMAmer attachment.[33] Another is translating the SOMAmer–protein binding event to a magnetic signal, which then can be detected via differential optical readout of an NV center. To address the second challenge, here we propose a protein binding assay that uses site-directed spin labeling of SOMAmers to generate a magnetic signal from a SOMAmer–protein binding event. Figure 1A illustrates the principles of this proposed mechanism. The unbound SOMAmer (apo state) is spin-labeled with a paramagnetic nitroxide radical ($S = 1/2$) at a specific nucleotide and is covalently attached to the diamond surface, proximal to an NV center. The spin label is incorporated at an appropriately chosen solvent-exposed site of the SOMAmer and is therefore rotationally mobile. When a target protein binds to a SOMAmer (holo state), the spin label's rotational mobility is reduced, and its distance to the NV center is possibly shifted. Both the rotational mobility change and the distance change affect the NV center spin–lattice relaxation rate, characterized by the longitudinal relaxation time constant T_1.[24,26,34] This rate can be measured using an optically detected magnetic resonance (ODMR) approach.[24,35–37]

For this detection mechanism to work, the spin-labeled SOMAmer must satisfy several prerequisites. First, the incorporation of the spin label must not degrade the SOMAmer–protein binding affinity; second, the spin label must undergo a significant rotational mobility or distance change upon protein binding; third, the rotational mobility or distance change must be on a scale that sensitively affects the NV center longitudinal relaxation rate. To identify sites that optimally satisfy these requirements, a complete scan of all spin labeling sites, i.e. all nucleotides, on a SOMAmer is necessary. While distance changes are only relevant in the presence of NV centers, rotational mobility changes can be measured using solution-state electron paramagnetic resonance (EPR) spectroscopy, a technique sensitive to molecular rotation rates on a time scale between 0.1 ns and 100 ns.[38]

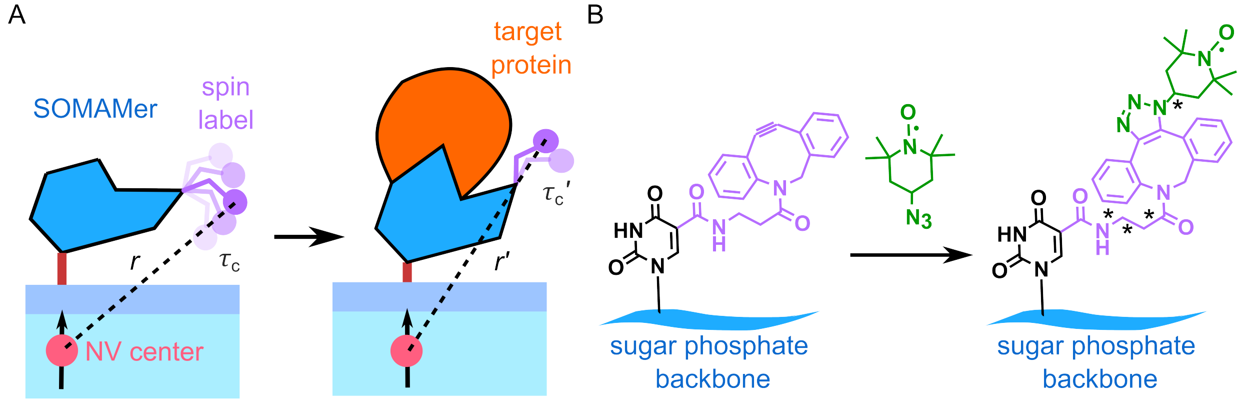

Figure 1: Schematic representation of NV-detected protein binding using spin-labeled SOMAmers. A. The apo and holo states of a SOMAmer covalently attached to the surface of a functionalized diamond via a linker (red). A spin label at distance r from the NV center is rotating with rate constant τ_c with little restriction. Protein binding potentially restricts and slows the rotational mobility and changes the distance from the spin label to the NV center. B. Chemical structures of uracil (black) modified with dibenzocyclooctyne (DBCO, purple) and nitroxide spin label (green). The asterisks indicate rotatable bonds. The spin label is incorporated via catalyst-free azide–alkyne cycloaddition.

In this work, we present a solution protein binding assay based on immobilized spin-labeled SOMAmers. We use a nitroxide-based spin label, since nitroxides are well-studied in solution EPR experiments and are sensitive reporters of molecular rotational motion.[39,40] The spin label is incorporated into a SOMAmer via site-specific azide–alkyne cycloaddition as shown in Figure 1B.[41,42] A model system was used for optimizing the spin labeling procedure and demonstrating the workflow for selecting labeling sites using two criteria: a small dissociation constant (K_d) and a large change in rotational mobility in response to protein binding, quantified by the rotational correlation time constant (τ_c) of a fitted Brownian rotational diffusion model. The model system consists of a SOMAmer named SL5 and its target protein, platelet-derived growth factor B (PDGF-BB dimer).[17] We performed binding affinity assays for all labeling sites on SL5 and identified 19 non-disruptive sites. The associated constructs were immobilized on agarose beads via streptavidin-biotin linkers. The rotational mobility changes were then evaluated using solution-state EPR spectroscopy combined with spectral simulations to obtain τ_c before and after addition of PDGF. Several site show a significant change τ_c, demonstrating the feasibility of this magnetically detected assay. Using the experimentally determined τ_c, we also model the impact of τ_c on NV center T_1 relaxation and discuss the effect of the NV center–spin label geometry on the overall robustness of a T_1 relaxometry-based detection mechanism.

Materials and methods

Spin-labeled SOMAmer preparation

An ABI 3900 automated DNA synthesizer (Applied Biosystems) was used with conventional phosphoramidite methods with minor changes to the coupling conditions for modified phosphoramidites. Modified phosphoramidites were used in 0.1 M solutions using acetonitrile with 0-40% dichloromethane and 0-20% sulfolane as the solvent. Solid support was an ABI-style fritted column packed with controlled pore glass (CPG, LGC Biosearch Technologies) loaded with 3'-DMT-dT succinate with 1000 Å pore size. All syntheses were performed at the 50 nmol scale and the 5' end of each sequence was modified with a hexaethylene glycol (HEG) spacer and biotin group for support attachment. Introduction of a DBCO-modified nucleotide variant was done as a single-base replacement at selected sites within the DNA strand using phosphoramidites synthesized by SomaLogic, Inc. Deprotection was accomplished by treatment with concentrated ammonium hydroxide at 55 °C for 4-6 hours, after which the product mixtures were filtered and residual solvents removed in a Genevac HT-12 evaporator. Identity and percent full-length product were determined using an Agilent 1290 Infinity LC system with an Agilent 6130B single quadrupole mass spectrometry detector using an Acquity C18 column 1.7 µM 2.1x100mm (Waters).

The resulting crude DBCO-modified SOMAmer residues were then redissolved in water for injection (WFI, HyPure WFI Quality Water, HyClone Laboratories, or equivalent) to 0.17 mM concentration (based on synthesis scale). A 100 mM solution of commercially sourced 4-azido-2,2,6,6-tetramethyl-piperidinyl-1-oxyl (TEMPO) azide (Glen Research 50-2007-92) was prepared in dimethyl sulfoxide. Each oligonucleotide mixture received an aliquot of the azide solution at a 4:1 ratio of azide to SOMAmer (based on synthesis scale) and the resulting mixture was mixed at room temperature for 24 to 65 hours, at which time analysis by LC/MS (Agilent 1290 Infinity, configured as above) confirmed that each cycloaddition reaction had reached completion (SI Figure S1). Each reaction mixture was then centrifugally filtered (Millipore Amicon Ultra-15 3K), washed three times with 5 mL WFI per wash for removal of small molecule impurities. Product was collected in approximately 500 µL WFI without further purification.

To spin label residues 1-4 and 11-29, we used the SL5 parent construct that contains a HEG linker in place of residues 5-10. To spin label residues 5-10, we used SL5 with the sequence GACZAC in place of the HEG linker, where Z is the modified nucleotide 5-benzylaminocarbonyl.[17] In this paper, the numbering is based on the 29-residue length.

Binding affinity measurements

To determine the K_d of modified aptamers, filter binding assays were performed using the SB18T binding buffer (40 mM HEPES, 102 mM NaCl, 5 mM KCl, 5 mM $MgCl_2$ and 0.01% Tween-20, pH 7.4). Modified aptamers were 5' end labelled using T4 polynucleotide kinase (New England Biolabs) and γ-[^{32}P]ATP (Perkin-Elmer). Radiolabeled aptamers ($\sim$20,000 cpm) were mixed with PDGF-BB (Creative BioMart) at concentrations ranging from 10^{-7} to 10^{-12} M and incubated at 37 °C for 40 minutes. Following incubation, 5.5 mL of 400 mg/mL silica-based microspheres (5 µM Zorbax PSM 300A, Cat. No. 899999-555, Agilent Technologies) was added, and bound complexes were captured on Durapore filter plates (EMD Millipore). The fraction of bound aptamer was quantified with a phosphoimager (Typhoon, GE Healthcare) and data were analyzed in ImageQuant (GE Healthcare).

Sample preparation for EPR measurements

The SOMAmer constructs used in EPR measurements were biotinylated[11] at the 5' end to facilitate immobilization on agarose beads coated with immobilized recombinant streptavidin protein (Pierce Streptavidin Plus UltraLink #53117; ThermoFisher Scientific). The bead diameter varies from 50 to 80 µm. SOMAmer concentration was determined by measuring the absorbance at 260 nm. Resin (0.5 mL of 50% slurry) was buffer exchanged into SB18T buffer, the supernatant was removed and 20 nmol of SOMAmer was applied to the resin. The reaction was incubated, with end-over-end rotation, at 37 °C for 1 hour. Resin was pelleted and supernatant was removed and discarded. Unbound streptavidin was quenched with 0.9 mL reaction buffer containing biotin. SOMAmer-loaded resin was washed thrice with 1 mL reaction buffer and resuspended in a final volume of 0.5 mL for a final concentration of 40 µM SOMAmer in 50% slurry. SOMAmer-loaded resin was stored at 4 °C. The PDGF-BB protein was stored at -80 °C then dissolved before use.

EPR measurements

Continuous-wave (CW) EPR experiments were performed with 40 µM SOMAmers in SB18T buffer. For the protein binding experiments, protein targets with concentration of 45-50 µM were added. For each sample, 12-15 µL were transferred into quartz capillaries (1.0 mm O.D. and 0.7 mm I.D.; Sutter Instrument). Solution-state EPR spectra were collected at room temperature (23 °C) using an X-band continuous-wave (CW) Bruker EMX spectrometer equipped with a ER 4123D dielectric resonator with a resonance frequency of 9.77 GHz. All spectra were obtained with a peak-to-peak modulation amplitude of 0.1 mT and a sweep rate of 0.24 mT/s and were collected under non-saturating conditions at 0.64 mW. Power saturation data are provided in the Supporting Information (SI Figure S2).

EPR spectral simulations

All spectra were aligned to the same magnetic field range and scaled by number of scans, receiver gain, and square root of power. Then, background was removed by subtracting the spectrum of buffer solution only. The spectra were integrated and normalized to obtain absorption spectra for simulation and comparison. An isotropic rigid-body Brownian rotational diffusion model[43,44] without motional restriction was fitted to the measured spectral lineshapes. The isotropic rotational correlation time τ_c and the g-tensor principal values (g_x, g_y, g_z) were varied for each fit. The hyperfine tensor principal values ($[A_x, A_y, A_z] = [21.79(3), 12.43(2), 103.01(2)]$ MHz) and the homogeneous broadening were simulated from a spectrum collected using a frozen solution of a free SOMAmer labeled at site 1 (SI Figure S4). Spectral simulations were performed using the open-source MATLAB toolbox EasySpin 6.0.0-dev.49,[45] with an example MATLAB script given in the SI (SI Section 2.3).

Results

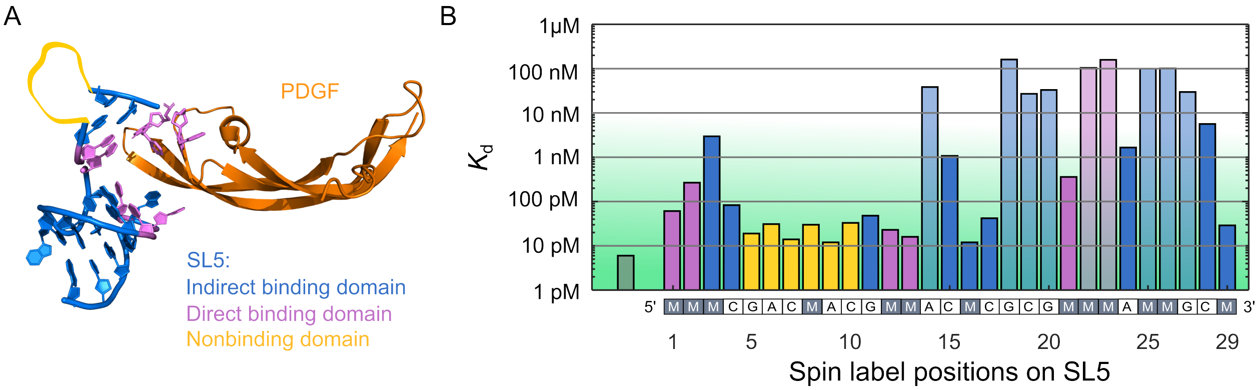

Figure 2: Evaluation of the binding affinity of spin-labeled SL5. A. A single SL5–PDGF-B complex from the crystal structure (PDBID 4hqu)[17] B. Binding affinity assay of SL5 spin-labeled at all nucleotides. The bottom row indicates the nucleotide sequence in the unlabeled construct, where "M" represents any non-canonical nucleotide. The K_d of unlabeled construct is 6 pM, indicated on the left in gray. The typical error in $\log_{10}(K_\mathrm{d})$ is about ± 0.15, i.e. an overall uncertainty for K_d of a factor of 2. The green shaded region represents the acceptable range (under 6 nM) with opacity representing tightness of binding. Sites with low affinity (paler color bars) were excluded from EPR measurements.

Binding affinity assay

To identify non-disruptive labeling sites, the binding affinities for PDGF of all SL5 constructs spin-labelled at each of the 29 sites were measured. The determined values of K_d are shown in Fig. 2. The measured K_d of the unlabeled SOMAmer is 6 pM (indicated on the left in Fig. 2). No spin-labeled construct binds to PDGF as tightly as the unlabeled parent SOMAmer. Based on a previously obtained crystal structure of SL5–PDGF complex, the labeling sites structurally fall into three domains: a direct binding domain, an indirect binding domain and a non-binding domain.[17] Incorporation of a spin label into any site in the non-binding domain (yellow) does not significantly disrupt the interaction since all K_d values in this region are under 100 pM. For the direct and indirect binding domains (purple and blue, respectively), no clear correlation between the physical location and the magnitude of K_d degradation is observed. Some site are highly disruptive (e.g. 18 and 23), whereas others (12, 13, 16) have K_d values similar to those with labelled sites in the non-binding domain. For the purpose of selecting optimal labeling sites for NV center detection, any construct with a K_d larger than 6 nM (1000-fold reduction compared to parent construct) was deemed too disruptive and excluded from further analysis. Site 29 was excluded as well, as spin labeling at this site was unsuccessful.

EPR measurements and rotational mobility analysis

To magnetically detect protein binding with the spin-labelled SOMAmers in solution, room-temperature EPR spectra were recorded before and after protein binding (SI Figure S3 bottom). The change in spectral shape is significant and is due to a change in the overall molecular size. This demonstrates the feasibility of this EPR-based solution binding assay. To mimic a diamond surface for potential optical readout of this assay, 19 biotinylated constructs that passed the binding affinity screening were ligated to streptavidin-coated agarose beads. This suppresses the global tumbling of the entire SOMAmer or SOMAmer–protein complex (SI Figure S3 top) and isolates the rotational motion of the spin label.

Again, spectra were recorded in the absence and presence of target protein (SI Figures S5 and S6). All spectra were analyzed as described above, and rotational correlation times τ_c were determined for all sites (SI Tables S2). Figure 3A shows an example using the construct labeled at site 12. Spin label rotational diffusion slows down after addition of the target protein PDGF as indicated by the broadening of the spectral lineshape in the low-field region around 346 mT (indicated by an arrow). This region of the spectrum corresponds to the $m_I = +1$ manifold of the ^{14}N nucleus of the nitroxide. Additionally, the high-field edge of the spectrum at about 351 mT sharpens slightly. Least-squares fits of simulated spectra to the experimental data reveal a significant increase in τ_c. The results for all sites, shown in Fig. 3C, indicate that significant changes in τ_c are observed for many sites.

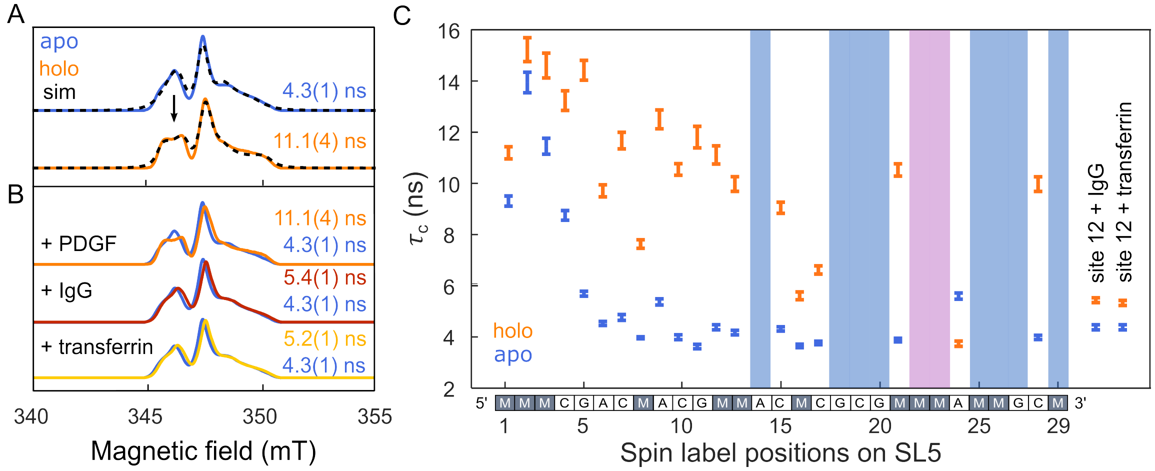

Figure 3: Evaluation of the mobility change of spin-labeled SL5 upon protein binding. A. An example of the integrated spectra for the apo (blue) and holo (orange) states of SL5 labeled at site 12 with simulated lineshapes obtained by fitting a rotational diffusion model. Fitted τ_c values are given in corresponding colors. The black arrow marks the feature that is most indicative of the mobility change. B. Control experiments using site 12 with non-target proteins IgG (red) and transferrin (yellow). C. Fitted τ_c values of for the apo and holo states of all EPR-evaluated constructs and for two non-target protein controls. The excluded sites are indicated by shaded columns with colors corresponding to Figure 2.

To evaluate the possible change in τ_c from non-specific bindings, control experiments were performed using the SOMAmer construct labeled at site 12 and two different non-target proteins: immunoglobulin G (IgG) and transferrin. The two non-target proteins were chosen for their high abundance in human plasma.[46] The results shown in Figure 3B indicate that the addition of non-target proteins do not significantly change τ_c. Small shifts are observed at the maxima of the holo spectra of PDGF and non-target proteins, possibly indicating changes in the g-tensor of the electron spin. The shifts could be attributed to the changes in the hydrogen-bonding environment around the nitroxide group of the spin label.[47] The slight increase in fitted τ_c from the apo to the holo state of the control experiments may be a result of the simple model used in the fitting.

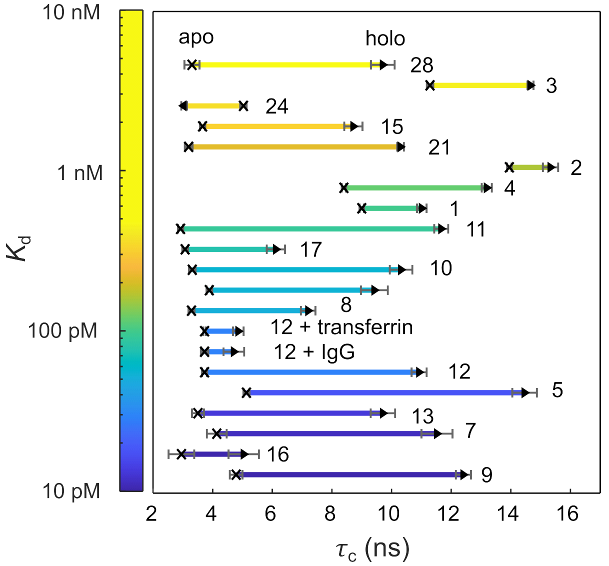

Figure 4: Evaluation of the performance of all spin-labeled SOMAmer constructs based on K_d (vertical axis) and τ_c (horizontal axis). The magnitude of the difference in τ_c between the apo (×) and holo (▶) states is indicated by arrow length, and the corresponding K_d values are indicated by arrow color according to the color bar on the left.

To compare both binding affinity and mobility changes observed from all sites, Figure 4 plots the values of τ_c before and after protein binding for all constructs along with their K_d as measured by the binding affinity assays. The experimentally determined τ_c are indicated by the corresponding markers, and the length of the arrow represents the magnitude of change in τ_c (denoted as $\Delta\tau_c$) after addition of protein. For the experiments using the target protein PDGF, sites 1, 2, 3 and 16 have the smallest $\Delta\tau_c$, whereas sites 5, 7, 9 and 11 have the largest. Site 24 is the only one that shows a decrease of rotational mobility upon binding; nonetheless, the difference is relatively small. Optimal labeling sites should have a large $\Delta\tau_c$ and a small K_d. Sites 5, 7, 9 and 12 best fit these criteria. Similar to the binding affinity screening results, there is no obvious correlation between the magnitude of rotational mobility change and the physical location of the labeling site since sites 5, 7 and 9 are all in the non-binding domain, and sites 12 and 13 are in the direct binding domain.

Overall, the results indicate that spin labels can be used as reporters of SOMAmer–protein binding and can therefore form the basis of protein sensors with high sensitivity and specificity.

Discussion

Next, we explore how the EPR-detected SOMAmer protein binding assay demonstrated above can be combined with fluorescence detection via diamond NV centers. Having experimentally determined the rotational correlation times τ_c, we can estimate the effect of protein binding on the T_1 relaxation time of an NV center in proximity to the spin-labeled SOMAmer using a previously published model.[24,26] In this model, the total T_1 relaxation rate of an NV center in proximity to a spin label is a sum of three independent contributions:

$$\frac{1}{T_1} = \frac{1}{T_1^0} + \frac{1}{T_1^{\mathrm{rot}}} + \frac{1}{T_1^{\mathrm{rlx}}}. \tag{1}$$

Here, $1/T_1^0$ is the NV center's intrinsic spin–lattice relaxation rate in the absence of the spin label, $1/T_1^{\mathrm{rot}}$ is the contribution from the rotational dynamics of the spin label, and $1/T_1^{\mathrm{rlx}}$ is the contribution from the spin label's own intrinsic spin relaxation dynamics.

The first term depends on temperature,[48,49] diamond surface quality,[50–52] depth of NV center from surface,[37,53] and the spin environment,[54] especially the ^{13}C concentration in the diamond lattice.[55,56] For a single NV center implanted in a ^{12}C isotopically purified diamond, T_1^0 can be as long as several milliseconds[37,57,58] at room temperature, whereas bulk NV centers in nanodiamonds may have T_1^0 as short as hundreds of µs at room temperature.[26,49,59]

The second term represents the effect of a fluctuating magnetic field at the NV center due to the rotational diffusion dynamics of the spin label, mediated by the dipolar coupling between spin label and NV center. At the appropriate frequency, this fluctuating field induces transitions at the NV center. The associated transition rate is given by

$$\frac{1}{T_1^{\mathrm{rot}}} = 3\gamma_{\mathrm{NV}}^2 B_{\perp,\mathrm{rot}}^2 J_{\tau_{\mathrm{c}}}(\omega_{\mathrm{NV}}), \tag{2}$$

where γ_{NV} is the gyromagnetic ratio of the NV center, $B_{\perp,\mathrm{rot}}$ is the averaged magnetic field generated by the spin label in the plane perpendicular to the magnetization direction of the NV center, and $J_{\tau_{\mathrm{c}}}(\omega_{\mathrm{NV}})$ is the spectral density of the rotating spin label evaluated at ω_{NV}, the angular frequency for the $m_s = 0 \leftrightarrow \pm 1$ transition of the NV center. The full derivation of this relation is given in the Supporting Information (SI section 3.2).

$B_{\perp,\mathrm{rot}}^2$ is given by

$$B_{\perp,\mathrm{rot}}^2 = \frac{1}{4}\left(\frac{\mu_0}{4\pi}\hbar\gamma_{\mathrm{SL}}\right)^2 \frac{2 + 3\sin^2\theta}{r^6}, \tag{3}$$

where μ_0 is the vacuum magnetic permeability, γ_{SL} is the gyromagnetic ratio of the spin label, r is the distance between the spin label and the NV center, and θ is the angle between the magnetization direction of the NV center in a weak external magnetic field and the NV–spin label direction. Via r and θ, $B_{\perp,\mathrm{rot}}^2$ contains the geometry dependence of $1/T_1$: the rate drops off rapidly with increasing distance, but is only mildly orientation dependent as the θ term varies beween 2 for $\theta = 0$ and 5 for $\theta = \pi/2$.

The spectral density in Eq. (2) is given by

$$J_{\tau_{\mathrm{c}}}(\omega) = \frac{\tau_{\mathrm{c}}}{1 + \tau_{\mathrm{c}}^2\omega^2}, \tag{4}$$

and represents the fluctuating field amplitude as a function of frequency ω. Its value at $\omega = \omega_{\mathrm{NV}}$ is used in Eq. (2).

The third term in Eq. (1) is the contribution from the relaxation dynamics of the spin label, which is relayed to the NV center by the same mechanisms as the second term. It contains several separate contributions:[60,61]

$$\frac{1}{T_1^{\mathrm{rlx}}} = \left(\frac{\mu_0}{4\pi}\right)^2 \gamma_{\mathrm{NV}}^2 \gamma_{\mathrm{SL}}^2 \hbar^2 \frac{1}{r^6} \left(\frac{1}{6}B + 3C + \frac{3}{2}E\right), \tag{5}$$

$$B = \frac{T_{2,\mathrm{SL}}}{1 + (\omega_{\mathrm{NV}} - \omega_{\mathrm{SL}})^2 T_{2,\mathrm{SL}}^2} (1 - 3\cos^2\theta)^2, \tag{6}$$

$$C = \frac{T_{1,\mathrm{SL}}}{1 + \omega_{\mathrm{NV}}^2 T_{1,\mathrm{SL}}^2} \sin^2\theta \cos^2\theta, \tag{7}$$

$$E = \frac{T_{2,\mathrm{SL}}}{1 + (\omega_{\mathrm{NV}} + \omega_{\mathrm{SL}})^2 T_{2,\mathrm{SL}}^2} \sin^4\theta, \tag{8}$$

where ω_{SL} is the (angular) transition frequency of the spin label electron, and $T_{1,\mathrm{SL}}$ and $T_{2,\mathrm{SL}}$ are the spin–lattice and spin–spin relaxation times of the spin label, respectively. Each of the three terms B, C and E is a product of a spectral density (depending on $T_{1,\mathrm{SL}}$ or $T_{2,\mathrm{SL}}$) and an angular term. Given a reasonable NV–spin label geometry ($r = 6$ nm and $\theta = 45°$) and typical ranges of relaxation times of nitroxides, 0.3 to 3 µs for T_1 and 0.1 to 1 µs for T_2,[62,63] values for $1/T_1^{\mathrm{rlx}}$ are significantly smaller than the T_1^0 relaxation rate (details are discussed in SI section 3.3). Therefore, the $1/T_1^{\mathrm{rlx}}$ term is negligible and is dropped from now on.

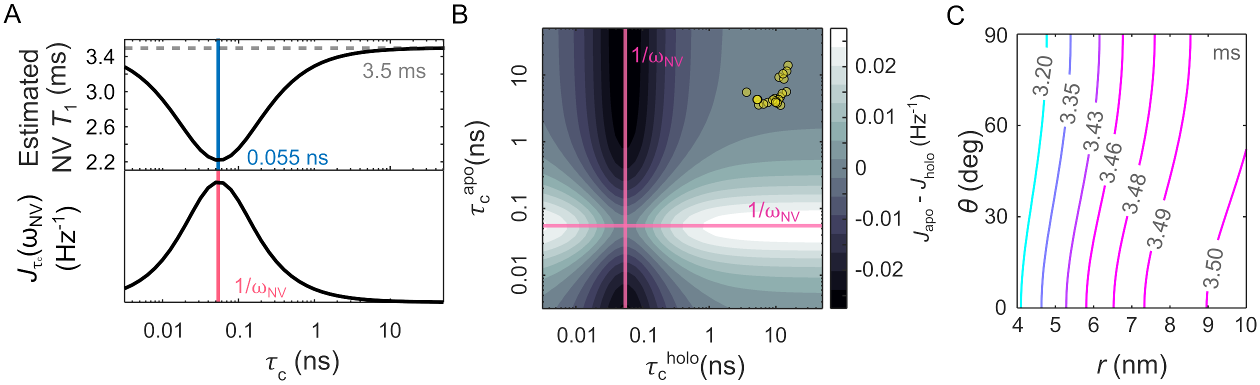

Figure 5: The predicted dependence of NV center T_1 on measured τ_c. A. Simulating the T_1 of the NV center as a function of τ_c. Top: estimated T_1 of an NV center 6 nm from the spin label, with a fixed angle $\theta = 45°$. Blue solid line: the minimum T_1 at $\tau_c = 0.055$ ns. Gray dotted line: the intrinsic T_1 of the NV center in the absence of a spin label, T_1^0. Bottom: the spectral density evaluated at ω_{NV}. Pink solid line: the maximum of the spectral density at $\tau_c = 1/\omega_{NV}$ B. The change in spectral density at ω_{NV} as a function of and apo and holo τ_c. The color bar indicates the differences between density amplitudes at two τ_c values. Yellow dots: τ_c values of apo and holo states of SL5 constructs. Pink solid line indicates $1/\omega_{NV}$. C. T_1 (ms) of the NV center a function of NV center–spin label distance and orientation. The contour lines represent NV center T_1 in the presence of a mobile spin label with $T_1^0 = 3.5$ ms and $\tau_c = 4$ ns at a location specified by distance r and angle θ.

Figure 5 elaborates on the dynamic and geometric aspects of $1/T_1^{\mathrm{rot}}$. Figure 5A illustrates the effect of τ_c for a fixed NV–spin label geometry (r and θ). The top panel shows estimated NV T_1 as a function of spin label τ_c from 0.01 ns to 50 ns, using the first two terms in Eq. (1) with $T_1^0 = 3.5$ ms, $r = 6$ nm and $\theta = 45°$. The bottom panel shows the spectral density from Eq. (4) as a function of τ_c. The spectral density can be used to infer the magnitude of T_1 reduction. The density amplitude quantifies the transition rate at the NV center due spin label reorienting at different rates. To isolate the dynamics of the spin label from the geometric factors, Figure 5B illustrates the effect of the τ_c values for the apo and the holo states on the change in spectral density (which is proportional to the change in relaxation rate). A large change in spectral density will enhance T_1 contrast. The largest spectral density changes occur if one of τ_c^{apo} and τ_c^{holo} is close to $1/\omega_{NV}$ and the other is at least an order of magnitude slower or faster (white and black regions in Figure 5B). The apo/holo τ_c values for SL5–PDGF are shown by the cluster of yellow dots. The τ_c values of apo and holo state range from 2.5-5 ns and 6-16 ns, respectively. They do not fall within the most sensitive range. One approach to improve upon this is to build more flexible linkers into the structure by exploring a wider range of spin label structures and coupling chemistries.

Figure 5C visualizes the dependence of T_1 on the relative position of the NV center spin and the nitroxide spin for a fixed τ_c. According to Eq. (3), T_1^{rot} contains an angular dependence and a factor of $1/r^6$, and the relaxation enhancement is most pronounced if the spin–spin distance is short and the angle θ perpendicular. The contour plot shows T_1 using $T_1^0 = 3.5$ ms and $\tau_c = 4$ ns. The reduction in T_1 increases as the angle θ approaches 90° and decreases with increasing distance. This is an important aspect for combining the spin-labeled SOMAmer assay with a diamond sensor since both orientation and distance affect the sensitivity of the T_1 relaxation-based sensing mechanism.

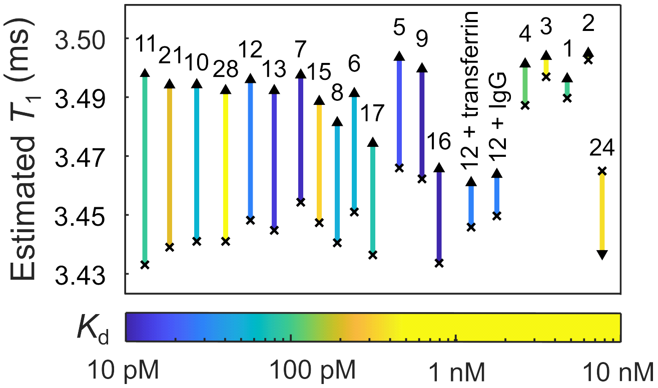

Figure 6: Evaluating the estimated $T_{1,\,\mathrm{NV}}$ for all tested sites, assuming $r = 6$ nm and $\theta = 45°$. The magnitude of the difference in $T_{1,\,\mathrm{NV}}$ between the apo (×) and holo (▲) states is indicated by arrow length, and the corresponding K_d is indicated by arrow color with a reference in Figure 4.

To evaluate the reduction of T_1 relaxation rate due to the protein binding-induced changes in rotational mobility for spin-labelled SL5, T_1 values are estimated for all sites using the same geometry ($r = 6$ nm and $\theta = 45°$) as used in Figure 5A. The calculated results are ranked from the largest to the smallest binding-induced T_1 change from left to right in Figure 6. In this geometry, the construct labelled at site 11 produces the largest contrast in T_1, followed by sites 21 and 10. However, sites 5, 7, 9 and 12, which yield the largest differences in τ_c, are not among the highest-ranked sites in terms of T_1 contrast. This is because the apo state τ_c of these constructs are longer than those of sites 11, 21 and 10 (Figure 4), resulting in a shorter window of $\Delta\tau_c$ as illustrated by Figure 5A.

The estimated ΔT_1 ranges from 0.05 ms (site 11) to less than 0.01 ms (site 1 through 4). Recent work has demonstrated a reliable resolution of 100 µs using nanodiamonds.[64] Several publications also managed to distinguish ΔT_1 values of hundreds of ms to tens of µs.[59,65–67] The SL5-PDGF binding-induced reduction of the estimated NV center ΔT_1 falls in a range that can be detected by current NV center sensor devices.[24,26,32,36,68,69] Nevertheless, several strategies can be applied to increase T_1 contrast and therefore the overall sensitivity of the NV center relaxometry.

NV center T_1 relaxometry detection sensitivity is strongly limited by the NV–spin label distance due to the steep $1/r^6$ dependence in Eq. (3). Therefore, keeping r as short as possible is crucial. The depth of the NV center below the diamond surface can be engineered via tuning the energy of ion implantation.[70,71] The caveat is that shallow NV centers are often susceptible to magnetic noise from surface spins.[51,52,57] Another approach to potentially increase ΔT_1 is to shorten the spin label linker length by using alternative labeling chemistries such as coupling of azide-functionalized spin labels with terminal alkynes[72] or strained cycloalkynes,[73] or by ligation to the phosphate group,[74] the sugar[75] and the base.[76–79] A series of rigid spin labels that can be covalently conjugated to the base were designed for measuring the flexibility of DNA;[76,80–84] however, these labels are less useful in this context, as their rigidity prevents the detection of spin label mobility changes. The τ_c screening protocol reported in this work relies on the built-in mobility from the rotatable bonds in the linker (Figure 1B). In addition to linker length and rigidity, linker size is another critical aspect. An inflexible and bulky linker may have greater potential to disrupt binding interactions in comparison to a small and compact structure. The ideal linker would be short but flexible so that the spin label is close to the SOMAmer and responsive to protein binding, but can still span a wide dynamic range of rotational motion.

The affinity of SOMAmer–protein binding may affect the overall sensitivity of the NV center detection. This effect is difficult to isolate and must be evaluated with the changes in spin label mobility upon protein binding. However, the SOMAmers may undergo conformational changes when binding to target proteins, potentially leading to distance changes. According to Eq. (3), the effect from a distance change can be as dramatic as the effect from a change in τ_c. The distance change may counteract or enhance the effect of the τ_c change on T_1. Further investigations of SOMAmer structure and conformational landscapes, also in the context of their attachment to a diamond surface,[33] will provide more information on probable distance effect.

Conclusions

We developed a novel protocol for sensing proteins using immobilized site-specifically spin-labeled SOMAmers in combination with CW EPR spectroscopy to detect changes in spin label rotational mobility upon protein binding. A full site scan on the benchmark SOMAmer SL5 and its target protein PDGF-BB revealed a number of suitable sites where (a) the binding-induced change in rotational mobility is significant and (b) the reduction in binding affinity due to the presence of the spin label is small. The approach presented here is general and can be extended to other SOMAmer–protein pairs.

In addition, we modeled the detection of the observed rotational mobility changes via T_1 relaxometry of a proximal diamond NV center, which provides a platform for increased sensitivity and multiplexing. The results indicate several strategies for maximizing contrast in NV T_1. First, minimize T_1 in the unbound state by shortening the rotational correlation time to approach the inverse angular transition frequency of the NV center. Second, maximize the slow-down of τ_c experienced by the spin label upon protein binding. Both strategies can be pursued by varying the nature of the spin label and scanning across labeling sites. Also, the NV–spin label distance needs to be carefully controlled in order to maximize T_1

contrast.

Acknowledgement

This work was supported by the National Science Foundation (ITE-2040520 to L.G., J.P.C. and S.S.; CHE-2154302 to S.S.).

Supporting Information Available

The Supporting Information contains the details of spin-labeled SOMAmer characterization, EPR experiments and derivation of the expression for T_1 of the NV center.

References

(1) Zhong, W.; Edfors, F.; Gummesson, A.; Bergström, G.; Fagerberg, L.; Uhlén, M. Next generation plasma proteome profiling to monitor health and disease. *Nat. Commun.* **2021**, *12*, 2493.

(2) Deutsch, E. W.; Omenn, G. S.; Sun, Z.; Maes, M.; Pernemalm, M.; Palaniappan, K. K.; Letunica, N.; Vandenbrouck, Y.; Brun, V.; Tao, S.-C.; Yu, X.; Geyer, P. E.; Ignjatovic, V.; Moritz, R. L.; Schwenk, J. M. Advances and Utility of the Human Plasma Proteome. *J. Proteome Res.* **2021**, *20*, 5241–5263.

(3) Singh, N. K.; Jain, P.; Das, S.; Goswami, P. Dye Coupled Aptamer-Captured Enzyme Catalyzed Reaction for Detection of Pan Malaria and P. falciparum Species in Laboratory Settings and Instrument-Free Paper-Based Platform. *Anal. Chem.* **2019**, *91*, 4213–4221.

(4) Senf, B.; Yeo, W. H.; Kim, J. H. Recent Advances in Portable Biosensors for Biomarker Detection in Body Fluids. *Biosensors* **2020**, *10*, 127.

(5) Ganguly, A.; Lin, K. C.; Muthukumar, S.; Prasad, S. Autonomous, Real-Time Monitoring Electrochemical Aptasensor for Circadian Tracking of Cortisol Hormone in Submicroliter Volumes of Passively Eluted Human Sweat. *ACS Sens.* **2021**, *6*, 63–72.

(6) Ren, X.; Gelinas, A. D.; von Carlowitz, I.; Janjic, N.; Pyle, A. M. Structural basis for IL-1α recognition by a modified DNA aptamer that specifically inhibits IL-1α signaling. *Nat. Commun.* **2017**, *8*, 810.

(7) Duo, J.; Chiriac, C.; Huang, R. Y.; Mehl, J.; Chen, G.; Tymiak, A.; Sabbatini, P.; Pillutla, R.; Zhang, Y. Slow Off-Rate Modified Aptamer (SOMAmer) as a Novel Reagent in Immunoassay Development for Accurate Soluble Glypican-3 Quantification in Clinical Samples. *Anal. Chem.* **2018**, *90*, 5162–5170.

(8) Jankowski, W.; Lagassé, H. A. D.; Chang, W. C.; McGill, J.; Jankowska, K. I.; Gelinas, A. D.; Janjic, N.; Sauna, Z. E. Modified aptamers as reagents to characterize recombinant human erythropoietin products. *Sci. Rep.* **2020**, *10*, 18593.

(9) Xu, X.; Zhang, C.; Denton, D. T.; O'Connell, D.; Drolet, D. W.; Geisbrecht, B. V. Inhibition of the Complement Alternative Pathway by Chemically Modified DNA Aptamers That Bind with Picomolar Affinity to Factor B. *J. Immunol.* **2021**, *206*, 861–873.

(10) Gold, L.; Ayers, D.; Bertino, J.; Bock, C.; Bock, A.; Brody, E. N.; Carter, J.; Dalby, A. B.; Eaton, B. E.; Fitzwater, T.; Flather, D.; Forbes, A.; Foreman, T.; Fowler, C.; Gawande, B.; Goss, M.; Gunn, M.; Gupta, S.; Halladay, D.; Heil, J.; Heilig, J.; Hicke, B.; Husar, G.; Janjic, N.; Jarvis, T.; Jennings, S.; Katilius, E.; Keeney, T. R.; Kim, N.; Koch, T. H.; Kraemer, S.; Kroiss, L.; Le, N.; Levine, D.; Lindsey, W.; Lollo, B.; Mayfield, W.; Mehan, M.; Mehler, R.; Nelson, S. K.; Nelson, M.; Nieuwlandt, D.; Nikrad, M.; Ochsner, U.; Ostroff, R. M.; Otis, M.; Parker, T.; Pietrasiewicz, S.; Resnicow, D. I.; Rohloff, J.; Sanders, G.; Sattin, S.; Schneider, D.; Singer, B.; Stanton, M.; Sterkel, A.; Stewart, A.; Stratford, S.; Vaught, J. D.; Vrkljan, M.; Walker, J. J.; Watrobka, M.; Waugh, S.; Weiss, A.; Wilcox, S. K.; Wolfson, A.; Wolk, S. K.; Zhang, C.; Zichi, D. Aptamer-based multiplexed proteomic technology for biomarker discovery. *PLoS ONE* **2010**, *5*, e15004.

(11) Kraemer, S.; Vaught, J. D.; Bock, C.; Gold, L.; Katilius, E.; Keeney, T. R.; Kim, N.; Saccomano, N. A.; Wilcox, S. K.; Zichi, D.; Sanders, G. M. From SOMAmer-Based Biomarker Discovery to Diagnostic and Clinical Applications: A SOMAmer-Based, Streamlined Multiplex Proteomic Assay. *PLoS ONE* **2011**, *6*, e26332.

(12) Elskens, J. P.; Elskens, J. M.; Madder, A. Chemical modification of aptamers for increased binding affinity in diagnostic applications: Current status and future prospects. *Int. J. Mol. Sci.* **2020**, *21*, 1–31.

(13) Gelinas, A. D.; Davies, D. R.; Edwards, T. E.; Rohlof, J. C.; Carter, J. D.; Zhang, C.; Gupta, S.; Ishikawa, Y.; Hirota, M.; Nakaishi, Y.; Jarvis, T. C.; Janjic, N. Crystal Structure of Interleukin-6 in Complex with a Modified Nucleic Acid Ligand. *J. Biol. Chem.* **2014**, *289*, 8720–8734.

(14) Gupta, S.; Hirota, M.; Waugh, S. M.; Murakami, I.; Suzuki, T.; Muraguchi, M.; Shibamori, M.; Ishikawa, Y.; Jarvis, T. C.; Carter, J. D.; Zhang, C.; Gawande, B.; Vrkljan, M.; Janjic, N.; Schneider, D. J. Chemically Modified DNA Aptamers Bind Interleukin-6 with High Affinity and Inhibit Signaling by Blocking Its Interaction with Interleukin-6 Receptor. *J. Biol. Chem.* **2014**, *289*, 8706–8719.

(15) Eid, C.; Palko, J. W.; Katilius, E.; Santiago, J. G. Rapid Slow Off-Rate Modified Aptamer (SOMAmer)-Based Detection of C-Reactive Protein Using Isotachophoresis and an Ionic Spacer. *Anal. Chem.* **2015**, *87*, 6736–6743.

(16) Aljohani, M. M.; Cialla-May, D.; Popp, J.; Chinnappan, R.; Al-Kattan, K.; Zourob, M. Aptamers: Potential Diagnostic and Therapeutic Agents for Blood Diseases. *Molecules* **2022**, *27*, 383.

(17) Davies, D. R.; Gelinas, A. D.; Zhang, C.; Rohlof, J. C.; Carter, J. D.; O'Connell, D.; Waugh, S. M.; Wolk, S. K.; Mayfield, W. S.; Burgin, A. B.; Edwards, T. E.; Stewart, L. J.; Gold, L.; Janjic, N.; Jarvis, T. C. Unique motifs and hydrophobic interactions shape the binding of modified DNA ligands to protein targets. *Proc. Natl. Acad. Sci. U.S.A.* **2012**, *109*, 19971–19976.

(18) Gelinas, A. D.; Davies, D. R.; Edwards, T. E.; Rohlof, J. C.; Carter, J. D.; Zhang, C.; Gupta, S.; Ishikawa, Y.; Hirota, M.; Nakaishi, Y.; Jarvis, T. C.; Janjic, N. Crystal structure of interleukin-6 in complex with a modified nucleic acid ligand. *J. Biol. Chem.* **2014**, *289*, 8720–8734.

(19) Jarvis, T. C.; Davies, D. R.; Hisaminato, A.; Resnicow, D. I.; Gupta, S.; Waugh, S. M.;

Nagabukuro, A.; Wadatsu, T.; Hishigaki, H.; Gawande, B.; Zhang, C.; Wolk, S. K.; Mayfield, W. S.; Nakaishi, Y.; Burgin, A. B.; Stewart, L. J.; Edwards, T. E.; Gelinas, A. D.; Schneider, D. J.; Janjic, N. Non-helical DNA Triplex Forms a Unique Aptamer Scaffold for High Affinity Recognition of Nerve Growth Factor. *Structure* **2015**, *23*, 1293–1304.

(20) Degen, C. L.; Reinhard, F.; Cappellaro, P. Quantum sensing. *Rev. Mod. Phys.* **2017**, *89*, 1–39.

(21) Allert, R. D.; Briegel, K. D.; Bucher, D. B. Advances in nano- and microscale NMR spectroscopy using diamond quantum sensors. *Chem. Commun.* **2022**, *58*, 8165–8181.

(22) Barry, J. F.; Schloss, J. M.; Bauch, E.; Turner, M. J.; Hart, C. A.; Pham, L. M.; Walsworth, R. L. Sensitivity optimization for NV-diamond magnetometry. *Rev. Mod. Phys.* **2020**, *92*, 015004.

(23) Sushkov, A. O.; Lovchinsky, I.; Chisholm, N.; Walsworth, R. L.; Park, H.; Lukin, M. D. Magnetic resonance detection of individual proton spins using quantum reporters. *Phys. Rev. Lett.* **2014**, *113*, 1–5.

(24) Tetienne, J. P.; Hingant, T.; Rondin, L.; Cavaillès, A.; Mayer, L.; Dantelle, G.; Gacoin, T.; Wrachtrup, J.; Roch, J. F.; Jacques, V. Spin relaxometry of single nitrogen-vacancy defects in diamond nanocrystals for magnetic noise sensing. *Phys. Rev. B* **2013**, *87*, 235436.

(25) DeVience, S. J.; Pham, L. M.; Lovchinsky, I.; Sushkov, A. O.; Bar-Gill, N.; Belthangady, C.; Casola, F.; Corbett, M.; Zhang, H.; Lukin, M.; Park, H.; Yacoby, A.; Walsworth, R. L. Nanoscale NMR spectroscopy and imaging of multiple nuclear species. *Nat. Nanotechnol.* **2015**, *10*, 129–134.

(26) Li, C.; Chen, M.; Lyzwa, D.; Cappellaro, P. All-Optical Quantum Sensing of Rotational Brownian Motion of Magnetic Molecules. *Nano Lett.* **2019**, *19*, 7342–7348.

(27) Shi, F.; Zhang, Q.; Wang, P.; Sun, H.; Wang, J.; Rong, X.; Chen, M.; Ju, C.; Reinhard, F.; Chen, H.; Wrachtrup, J.; Wang, J.; Du, J. Single-protein spin resonance spectroscopy under ambient conditions. *Science* **2015**, *347*, 1135–1138.

(28) Akiel, R. D.; Zhang, X.; Abeywardana, C.; Stepanov, V.; Qin, P. Z.; Takahashi, S. Investigating functional DNA grafted on nanodiamond surface using site-directed spin labeling and electron paramagnetic resonance spectroscopy. *J. Phys. Chem. B* **2016**, *120*, 4003–4008.

(29) Lovchinsky, I.; Sushkov, A. O.; Urbach, E.; de Leon, N. P.; Choi, S.; De Greve, K.; Evans, R.; Gertner, R.; Bersin, E.; Müller, C.; McGuinness, L.; Jelezko, F.; Walsworth, R. L.; Park, H.; Lukin, M. D. Nuclear magnetic resonance detection and spectroscopy of single proteins using quantum logic. *Science* **2016**, *351*, 836–841.

(30) Shi, F.; Kong, F.; Zhao, P.; Zhang, X.; Chen, M.; Chen, S.; Zhang, Q.; Wang, M.; Ye, X.; Wang, Z.; Qin, Z.; Rong, X.; Su, J.; Wang, P.; Qin, P. Z.; Du, J. Single-DNA electron spin resonance spectroscopy in aqueous solutions. *Nat. Methods* **2018**, *15*, 697–699.

(31) Miller, B. S.; Bezinge, L.; Gliddon, H. D.; Huang, D.; Dold, G.; Gray, E. R.; Heaney, J.; Dobson, P. J.; Nastouli, E.; Morton, J. J.; McKendry, R. A. Spin-enhanced nanodiamond biosensing for ultrasensitive diagnostics. *Nature* **2020**, *587*, 588–593.

(32) Li, C.; Soleyman, R.; Kohandel, M.; Cappellaro, P. SARS-CoV-2 Quantum Sensor Based on Nitrogen-Vacancy Centers in Diamond. *Nano Lett.* **2022**, *22*, 43–49.

(33) Xie, M.; Yu, X.; Rodgers, L. V. H.; Xu, D.; Chi-Durán, I.; Toros, A.; Quack, N.; de Leon, N. P.; Maurer, P. C. Biocompatible surface functionalization architecture for a diamond quantum sensor. *Proc. Natl. Acad. Sci. U.S.A.* **2022**, *119*, e2114186119.

(34) Ariyaratne, A.; Bluvstein, D.; Myers, B. A.; Jayich, A. C. Nanoscale electrical conduc-

tivity imaging using a nitrogen-vacancy center in diamond. *Nat. Commun.* **2018**, *9*, 1–7.

(35) Hall, L. T.; Cole, J. H.; Hill, C. D.; Hollenberg, L. C. L. Sensing of Fluctuating Nanoscale Magnetic Fields Using Nitrogen–Vacancy Centers in Diamond. *Phys. Rev. Lett.* **2009**, *103*, 220802.

(36) Steinert, S.; Ziem, F.; Hall, L. T.; Zappe, A.; Schweikert, M.; Götz, N.; Aird, A.; Balasubramanian, G.; Hollenberg, L.; Wrachtrup, J. Magnetic spin imaging under ambient conditions with sub-cellular resolution. *Nat. Commun.* **2013**, *4*, 1607.

(37) Bluvstein, D.; Zhang, Z.; Jayich, A. C. B. Identifying and Mitigating Charge Instabilities in Shallow Diamond Nitrogen-Vacancy Centers. *Phys. Rev. Lett.* **2019**, *122*, 76101.

(38) Bordignon, E. In *EPR Spectroscopy: Fundamentals and Methods*; Goldfarb, D., Stoll, S., Eds.; John Wiley & Sons, Ltd: Chichester, UK, 2017; Chapter 6, pp 235–254.

(39) Hubbell, W. L.; Cafiso, D. S.; Altenbach, C. Identifying conformational changes with site-directed spin labeling. *Nat. Struct. Mol. Biol.* **2000**, *7*, 735–739.

(40) Feix, J. B.; Klug, C. S. In *Biological magnetic resonance*; Berliner, L. J., Ed.; Springer US: Boston, MA, 2002; Vol. 14; pp 251–281.

(41) Agard, N. J.; Prescher, J. A.; Bertozzi, C. R. A strain-promoted [3 + 2] azide-alkyne cycloaddition for covalent modification of biomolecules in living systems. *J. Am. Chem. Soc.* **2004**, *126*, 15046–15047.

(42) Kálai, T.; Hubbell, W. L.; Hideg, K. Click reactions with nitroxides. *Synthesis* **2009**, 1336–1340.

(43) Polnaszek, C. F.; Bruno, G. V.; Freed, J. H. ESR line shapes in the slow-motional region: Anisotropic liquids. *J. Chem. Phys* **1973**, *58*, 3185–3199.

(44) Schneider, D. J.; Freed, J. H. In *Spin Labeling: Theory and Applications*; Berliner, L., Reuben, J., Eds.; Springer US: Boston, MA, 1989; Vol. 8; pp 1–76.

(45) Stoll, S.; Schweiger, A. EasySpin, a comprehensive software package for spectral simulation and analysis in EPR. *J. Magn. Reson.* **2006**, *178*, 42–55.

(46) Anderson, N. L.; Anderson, N. G. The Human Plasma Proteome: History, Character, and Diagnostic Prospects. *Mol. Cell Proteomics* **2002**, *1*, 845–867.

(47) Bordignon, E.; Brutlach, H.; Urban, L.; Hideg, K.; Savitsky, A.; Schnegg, A.; Gast, P.; Engelhard, M.; Groenen, E. J. J.; Möbius, K.; Steinhoff, H.-J. Heterogeneity in the Nitroxide Micro-Environment: Polarity and Proticity Effects in Spin-Labeled Proteins Studied by Multi-Frequency EPR. *Appl. Magn. Reson.* **2010**, *37*, 391–403.

(48) Jarmola, A.; Acosta, V. M.; Jensen, K.; Chemerisov, S.; Budker, D. Temperature- and Magnetic Field Dependent Longitudinal Spin Relaxation in Nitrogen Vacancy Ensembles in Diamond. *Phys. Rev. Lett.* **2012**, *108*, 197601.

(49) de Guillebon, T.; Vindolet, B.; Roch, J.-F.; Jacques, V.; Rondin, L. Temperature dependence of the longitudinal spin relaxation time T_1 of single nitrogen-vacancy centers in nanodiamonds. *Phys. Rev. B* **2020**, *102*, 165427.

(50) Fávaro de Oliveira, F.; Antonov, D.; Wang, Y.; Neumann, P.; Momenzadeh, S. A.; Häußermann, T.; Pasquarelli, A.; Denisenko, A.; Wrachtrup, J. Tailoring spin defects in diamond by lattice charging. *Nat. Commun.* **2017**, *8*, 15409.

(51) Myers, B. A.; Das, A.; Dartiailh, M. C.; Ohno, K.; Awschalom, D. D.; Bleszynski Jayich, A. C. Probing Surface Noise with Depth-Calibrated Spins in Diamond. *Phys. Rev. Lett.* **2014**, *113*, 027602.

(52) Sangtawesin, S.; Dwyer, B. L.; Srinivasan, S.; Allred, J. J.; Rodgers, L. V.; De Greve, K.; Stacey, A.; Dontschuk, N.; O'Donnell, K. M.; Hu, D.; Evans, D. A.; Jaye, C.; Fis-

cher, D. A.; Markham, M. L.; Twitchen, D. J.; Park, H.; Lukin, M. D.; de Leon, N. P. Origins of Diamond Surface Noise Probed by Correlating Single-Spin Measurements with Surface Spectroscopy. *Phys. Rev. X* **2019**, *9*, 031052.

(53) Pham, L. M.; DeVience, S. J.; Casola, F.; Lovchinsky, I.; Sushkov, A. O.; Bersin, E.; Lee, J.; Urbach, E.; Cappellaro, P.; Park, H.; Yacoby, A.; Lukin, M.; Walsworth, R. L. NMR technique for determining the depth of shallow nitrogen-vacancy centers in diamond. *Phys. Rev. B* **2016**, *93*, 045425.

(54) Mrózek, M.; Rudnicki, D.; Kehayias, P.; Jarmola, A.; Budker, D.; Gawlik, W. Longitudinal spin relaxation in nitrogen-vacancy ensembles in diamond. *EPJ Quantum Technol.* **2015**, *2*.

(55) Balasubramanian, G.; Neumann, P.; Twitchen, D.; Markham, M.; Kolesov, R.; Mizuochi, N.; Isoya, J.; Achard, J.; Beck, J.; Tissler, J.; Jacques, V.; Hemmer, P. R.; Jelezko, F.; Wrachtrup, J. Ultralong spin coherence time in isotopically engineered diamond. *Nat. Mater.* **2009**, *8*, 383–387.

(56) Mizuochi, N.; Neumann, P.; Rempp, F.; Beck, J.; Jacques, V.; Siyushev, P.; Nakamura, K.; Twitchen, D. J.; Watanabe, H.; Yamasaki, S.; Jelezko, F.; Wrachtrup, J. Coherence of single spins coupled to a nuclear spin bath of varying density. *Phys. Rev. B* **2009**, *80*, 041201.

(57) Rosskopf, T.; Dussaux, A.; Ohashi, K.; Loretz, M.; Schirhagl, R.; Watanabe, H.; Shikata, S.; Itoh, K. M.; Degen, C. L. Investigation of Surface Magnetic Noise by Shallow Spins in Diamond. *Phys. Rev. Lett.* **2014**, *112*, 147602.

(58) Chen, J.; Chen, O. Y.; Chang, H. C. Relaxation of a dense ensemble of spins in diamond under a continuous microwave driving field. *Sci. Rep.* **2021**, *11*, 16278.

(59) Perona Martínez, F.; Nusantara, A. C.; Chipaux, M.; Padamati, S. K.; Schirhagl, R. Nanodiamond Relaxometry-Based Detection of Free-Radical Species When Produced

in Chemical Reactions in Biologically Relevant Conditions. *ACS Sens.* **2020**, *5*, 3862–3869.

(60) Goodman, G.; Leigh, J. S. Distance between the electron paramagnetic resonance-visible copper and cytochrome a in bovine heart cytochrome oxidase. *Biochemistry* **1985**, *24*, 2310–2317.

(61) Hirsh, D. J.; Beck, W. F.; Innes, J. B.; Brudvig, G. W. Using Saturation-Recovery EPR to Measure Distances in Proteins: Applications to Photosystem II. *Biochemistry* **1992**, *31*, 532–541.

(62) Eaton, G. R.; Eaton, S. S. Distance Measurements in Biological Systems by EPR. *Biological Magnetic Resonance* **2000**, *19*, 29–129.

(63) Schwartz, R. N.; Jones, L. L.; Bowman, M. K. Electron spin echo studies of nitroxide free radicals in liquids. *J. Phys. Chem.* **1979**, *83*, 3429–3434.

(64) Sigaeva, A.; Shirzad, H.; Perona Martinez, F.; Nusantara, A. C.; Mougios, N.; Chipaux, M.; Schirhagl, R. Diamond-Based Nanoscale Quantum Relaxometry for Sensing Free Radical Production in Cells. *Small* **2022**, *18*, 2105750–2105762.

(65) Barton, J.; Gulka, M.; Tarabek, J.; Mindarava, Y.; Wang, Z.; Schimer, J.; Raabova, H.; Bednar, J.; Plenio, M. B.; Jelezko, F.; Nesladek, M.; Cigler, P. Nanoscale dynamic readout of a chemical redox process using radicals coupled with nitrogen-vacancy centers in nanodiamonds. *ACS Nano* **2020**, *14*, 12938–12950.

(66) Gorrini, F.; Giri, R.; Avalos, C. E.; Tambalo, S.; Mannucci, S.; Basso, L.; Bazzanella, N.; Dorigoni, C.; Cazzanelli, M.; Marzola, P.; Miotello, A.; Bifone, A. Fast and Sensitive Detection of Paramagnetic Species Using Coupled Charge and Spin Dynamics in Strongly Fluorescent Nanodiamonds. *ACS Appl. Mater. Interfaces* **2019**, *11*, 24412–24422.

(67) Finco, A.; Haykal, A.; Tanos, R.; Fabre, F.; Chouaieb, S.; Akhtar, W.; Robert-Philip, I.; Legrand, W.; Ajejas, F.; Bouzehouane, K.; Reyren, N.; Devolder, T.; Adam, J.-P.; Kim, J.-V.; Cros, V.; Jacques, V. Imaging non-collinear antiferromagnetic textures via single spin relaxometry. *Nat. Commun.* **2021**, *12*, 1–6.

(68) Ziem, F. C.; Götz, N. S.; Zappe, A.; Steinert, S.; Wrachtrup, J. Highly Sensitive Detection of Physiological Spins in a Microfluidic Device. *Nano Lett.* **2013**, *13*, 4093–4098.

(69) Zhang, T.; Pramanik, G.; Zhang, K.; Gulka, M.; Wang, L.; Jing, J.; Xu, F.; Li, Z.; Wei, Q.; Cigler, P.; Chu, Z. Toward Quantitative Bio-sensing with Nitrogen-Vacancy Center in Diamond. *ACS Sens.* **2021**, *6*, 2077–2107.

(70) Fukuda, R.; Balasubramanian, P.; Higashimata, I.; Koike, G.; Okada, T.; Kagami, R.; Teraji, T.; Onoda, S.; Haruyama, M.; Yamada, K.; Inaba, M.; Yamano, H.; Stürner, F. M.; Schmitt, S.; McGuinness, L. P.; Jelezko, F.; Ohshima, T.; Shinada, T.; Kawarada, H.; Kada, W.; Hanaizumi, O.; Tanii, T.; Isoya, J. Lithographically engineered shallow nitrogen-vacancy centers in diamond for external nuclear spin sensing. *New J. Phys.* **2018**, *20*, 083029.

(71) Alghannam, F.; Hemmer, P. Engineering of Shallow Layers of Nitrogen Vacancy Colour Centres in Diamond Using Plasma Immersion Ion Implantation. *Sci. Rep.* **2019**, *9*, 5870.

(72) Winz, M.-L.; Linder, E. C.; André, T.; Becker, J.; Jäschke, A. Nucleotidyl transferase assisted DNA labeling with different click chemistries. *Nucleic Acids Res.* **2015**, e110.

(73) Kucher, S.; Korneev, S.; Tyagi, S.; Apfelbaum, R.; Grohmann, D.; Lemke, E. A.; Klare, J. P.; Steinhoff, H.-J.; Klose, D. Orthogonal spin labeling using click chemistry for in vitro and in vivo applications. *J. Magn. Reson.* **2017**, *275*, 38–45.

(74) Qin, P. Z.; Butcher, S. E.; Feigon, J.; Hubbell, W. L. Quantitative analysis of the

isolated GAAA tetraloop/receptor interaction in solution: A site-directed spin labeling study. *Biochemistry* **2001**, *40*, 6929–6936.

(75) Edwards, T. E.; Okonogi, T. M.; Robinson, B. H.; Sigurdsson, S. T. Site-Specific Incorporation of Nitroxide Spin Labels into Internal Sites of the TAR-RNA Structure Dependent Dynamics of RNA by EPR Spectroscopy. *J. Am. Chem. Soc.* **2001**, *123*, 1527–1528.

(76) Marko, A.; Margraf, D.; Cekan, P.; Sigurdsson, S. T.; Schiemann, O.; Prisner, T. F. Analytical method to determine the orientation of rigid spin labels in DNA. *Phys. Rev. E* **2010**, *81*, 021911.

(77) Wang, Y.; Kathiresan, V.; Chen, Y.; Hu, Y.; Jiang, W.; Bai, G.; Liu, G.; Qin, P. Z.; Fang, X. Posttranscriptional site-directed spin labeling of large RNAs with an unnatural base pair system under non-denaturing conditions. *Chem. Sci.* **2020**, *11*, 9655–9664.

(78) Krell, K.; Pfeuffer, B.; Rönicke, F.; Chinoy, Z. S.; Favre, C.; Friscourt, F.; Wagenknecht, H.-A. Fast and Efficient Postsynthetic DNA Labeling in Cells by Means of Strain-Promoted Sydnone-Alkyne Cycloadditions. *Chem. Eur. J.* **2021**, 16093–1609.

(79) Hu, Y.; Wang, Y.; Singh, J.; Sun, R.; Xu, L.; Niu, X.; Huang, K.; Bai, G.; Liu, G.; Zuo, X.; Chen, C.; Qin, P. Z.; Fang, X. Phosphorothioate-Based Site-Specific Labeling of Large RNAs for Structural and Dynamic Studies. *ACS Chem. Biol.* **2022**, *17*, 2448–2460.

(80) Miller, T. R.; Alley, S. C.; Reese, A. W.; Solomon, M. S.; McCallister, W. V.; Mailer, C.; Robinson, B. H.; Hopkins, P. B. A Probe for Sequence-Dependent Nucleic Acid Dynamics. *J. Am. Chem. Soc.* **1995**, *117*, 9377–9378.

(81) Margraf, D.; Cekan, P.; Prisner, T. F.; Sigurdsson, S. T.; Schiemann, O. Ferro- and antiferromagnetic exchange coupling constants in PELDOR spectra. *Phys. Chem. Chem. Phys.* **2009**, *11*, 6708–6714.

(82) Nguyen, P.; Shi, X.; Sigurdsson, S. T.; Herschlag, D.; Qin, P. Z. A single-stranded junction modulates nanosecond motional ordering of the substrate recognition duplex of a group i ribozyme. *ChemBioChem* **2013**, *14*, 1720–1723.

(83) Gophane, D. B.; Sigurdsson, S. T. Hydrogen-bonding controlled rigidity of an isoindoline-derived nitroxide spin label for nucleic acids. *Chem. Commun.* **2013**, *49*, 999–1001.

(84) Juliusson, H. Y.; Sigurdsson, S. T. Reduction Resistant and Rigid Nitroxide Spin-Labels for DNA and RNA. *J. Org. Chem.* **2020**, *85*, 4036–4046.

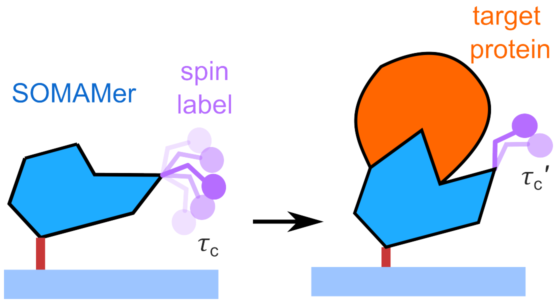

For TOC only